Final Draft

of the original manuscript

Xu, P.; Pyczak, F.; Yan, M.; Kong, F.; Ebel, T.:

Impacts of yttrium on microstructure and tensile properties of biomedical β Ti-Nb-Zr fabricated by metal injection molding.

In: Materials Science and Engineering: A. Vol. 792 (2020) 139816.

First published online by Elsevier: 27.06.2020

https://dx.doi.org/10.1016/j.msea.2020.139816

Impacts of yttrium on microstructure and tensile properties of biomedical β Ti-Nb-Zr fabricated by metal injection molding

Peng Xu[a, *], Florian Pyczak[a, b], Ming Yan[a, c], Fantao Kong[d], Thomas Ebel[a]

[a] Institute of Materials Research, Helmholtz-Zentrum Geesthacht, Max-Planck-Str. 1, Geesthacht D-21502, Germany

[b] Brandenburgisch Technische Universität Cottbus-Senftenberg, Konrad-Wachsmann-Allee 17, Cottbus D-03046, Germany

[c] Department of Materials Science and Engineering, Southern University of Science and Technology, Shenzhen 518055, P.R. China

[d] School of Materials Science and Engineering, Harbin Institute of Technology, West Dazhi Road 92, Harbin 150001, P.R. China

Corresponding author: Peng Xu (P. Xu), email address: peng.xu@hzg.de

Abstract: Impurities, particularly oxygen, are a critical issue to address in metal-injection-molding (MIM) processed Ti-Nb-Zr biomaterials. The addition of rare earth (RE) elements such as yttrium is a possible solution to the impurity problem due to their potential for scavenging oxygen. The impacts of added Y on the sinterability, microstructure and mechanical properties of the MIMed Ti-Nb-Zr, however, largely remain unclear. In this study, different sized Y particles with varying weight fractions have been added to the β Ti-Nb-Zr alloy in order to elucidate the aforementioned aspects. It has been found that, although the added Y has an obvious β grain refinement effect, its impacts on the residual porosity, ultimate tensile strength and tensile toughness can be significantly negative, particularly if using large sized Y particles. Small sized (<15 μm), moderate amount (e.g. 0.3 wt.%) of Y addition, however, proved to be beneficial, in terms of scavenging oxygen and promoting fracture toughness. Characterisation techniques and mechanical testing are employed to understand the above experimental findings with the assistance of sintering theory and existing literature. It is hoped that the present study can provide an important guidance for using Y as an oxygen scavenger to develop low-cost, high-performance MIMed Ti alloys.

Keywords: Metal injection molding; Titanium alloys; Yttrium; Oxygen scavenging; Particle size; Sinterability

1. Introduction

In the past decades, there has been continuously increasing research on a variety of advanced structural materials where rare earth (RE) elements were added to improve their mechanical properties or to realize specific functionalities [1-6]. The effects of RE additions to improve materials properties of titanium and its alloys can be summarized into at least the following three categories:

a. A small amount of RE addition is capable to effectively affect mechanical properties of various materials through precipitation hardening [7-9]. For instance, RE has been introduced into unalloyed titanium and various titanium alloys for achieving enhanced mechanical performance at both room temperature and elevated temperatures. The alloys were processed by rapid solidification [10], forging [11], selective electron beam melting [12], metal injection molding [13] and so forth;

b. The presence of RE containing ceramic-phases is capable to refine the grain size of titanium alloys by heterogeneous nucleation, grain boundary pinning and/or growth restriction at high temperature [14-17]. The resultant mechanical properties are much better than those without RE addition. In particular, microstructure refinement is of crucial importance for ensuring good fatigue performance of Ti alloys [18]. Thus, grain refinement is one of the reasons why RE has been introduced to powder metallurgy (PM) of titanium alloys that generally have a coarse-grained structure [19-21].

c. Different from ingot metallurgy (IM), oxygen contamination is not readily controllable in most PM-Ti alloys. It is well known that some important engineering materials such as Ti-6Al-4V and intermetallic Ti-Al display quite low tolerances for oxygen [22, 23]. For instance, a critical oxygen content of 3300 ppm (0.33 wt.%) is determined as the tough-brittle transition limit for the Ti-6Al-4V alloys [23]. This value can be even lower (1500−2200 ppm [24]) in the case of additively manufactured Ti-6Al-4V, if the microstructure consists of α′ martensitic phase. Oxygen degrades the ductility of titanium alloys via multiple mechanisms as summarized in the ref. [24]. To scavenge oxygen from Ti and mitigate its detrimental impact, a variety of RE elements have proven to be effective. It is shown that adding a small amount of RE can markedly increase the ductility of PM-Ti alloys by 60%−90% [21, 25].

As an important PM technology, metal injection molding (MIM) of titanium alloys attracts interests from both academy and industry, due to its capability to provide mass-produced, cost-effective, complex shaped and high performance Ti components [26-28]. In recent years, there is a tendency under the commercialization pressure to develop cost-affordable MIM Ti products using low cost feedstock/raw powder materials [29]. Hydride-dehydride (HDH) pure Ti powder made directly from Kroll sponge is being considered for use due to its very low price [30], i.e. USD $15/kg to $40/kg [31, 32]. The problem is that it normally contains as high as 2500 ppm oxygen content [21]. Aside from the raw Ti powder, an extra oxygen uptake of 800−1000 ppm

(300−500 ppm by careful handling [33]), occurs in most MIM processes due to the contamination of sintering atmosphere [34], powder (or feedstock) handling [21, 33], improper binder pyrolysis [26, 35], etc. Oxygen from alloying elements, such as strong β-phase stabilizer Nb and weak β-phase stabilizers like Zr, Ta and Hf [36, 37], may also possess high oxygen levels (e.g. gas-atomized Nb <45 μm ≈2200 ppm, Zr <45 μm ≈5000 ppm).

To mitigate the oxygen problem, Y (yttrium) is a plausible choice, according to the oxygen scavenging capability of REs: Y > Er > Dy > Tb > Gd [38, 39] and its low cost [40]. The Ellingham diagram [41] confirms that Y_2O_3 (yttria) has a lower formation energy than TiO_2, suggesting it can effectively scavenge oxygen from the Ti-matrix. A successful example of using Y for this purpose can be found in [42], which shows that MIMed Ti-6Al-4V alloys containing more than 4000 ppm oxygen can be fabricated by using inexpensive HDH master alloy powder (USD $25/kg) and 0.5 wt.% yttrium addition (USD $800/kg) with excellent tensile properties (UTS of 939 MPa, ε_f of 13.5%).

Y addition, however, may lead to an adverse effect, which is a higher amount of porosity [16]. It is well known that such a high amount of residual porosity can degrade the tensile properties [43-45]. It is suspected that the increase of porosity induced by Y addition is linked to the particle size of the used RE elemental powder. This issue still remains unclear to date. Also, no

systematic work was performed on the combined effect of oxygen scavenging, microstructure refinement and porosity increase caused by Y addition on the tensile properties of β Ti biomaterials, such as Ti-Nb-Zr with high oxygen contents (>2500 ppm). To develop cost-affordable, high-performance MIMed biomedical Ti alloys, it is quite important to understand the impacts of Y on the sinterability, microstructure and tensile properties.

This study investigates the effects of Y, added to scavenge oxygen and refine the prior β-grain size, on the resultant porosity and tensile properties in MIMed biomedical β Ti alloys with refractory alloying elements (Nb, Zr) and high impurity levels (oxygen > 2500 ppm, oxygen equivalent $O_{eq.}$ ≈4600 ppm). In particular, the critical particle size of Y elemental powder that leads to increased porosity (or degraded sinterability) is studied.

2. Experimental procedures

2.1. MIM processing

For the present study, feedstocks consisting of 65 vol.% metallic powders and 35 vol.% of wax-based binder were prepared. The alloy compositions (i.e. Ti-20Nb-10Zr-xY, x = 0, 0.3, 0.5, 0.7, 1; all in wt.%) are denoted as Ti2010, Ti2010-0.3Y, Ti2010-0.5Y, Ti2010-0.7Y and Ti2010-1Y throughout this article. Regarding the metallic powders, gas-atomized Grade 1 CP-Ti spherical powder with a particle size of less than 45 μm was supplied from TLS Technik, Germany;

master-alloyed Ti-42Nb spherical powder (<63 μm) was produced by H.C. Starck, Germany; and Zr and Y irregular elemental powders (both <45 μm) were commercially obtained from abcr GmbH, Germany and Edgetech, USA. The composition of the binder system was 35 wt.% ethylene vinyl acetate, 60 wt.% paraffin wax and 5 wt.% stearic acid. The binder system had been applied successfully before to MIM of other titanium alloys and Ti-Al intermetallic resulting in sound mechanical properties [46-49]. The aforementioned mixtures of feedstock (i.e. metallic powder + polymeric binder) were mixed in a double sigma-blades kneader (Femix KM 0.5K, Misch- und Knettechnik GmbH, Germany) for 4 h at 120 °C under protection of argon atmosphere. H_2O < 1 ppm and O_2 < 1 ppm, purified by a gas purification system (Böhler Ag, Austria).

According to the ISO 2740 standard, “dog bone” shaped tensile specimens were injection molded by using a conventional ARBURG 320 S machine. A maximum injection pressure of 135 MPa and an injection nozzle temperature of 112 °C were adopted during processing. For this binder system, a two-stage debinding process was conducted afterwards: chemical debinding firstly extracted the paraffin wax, and then thermal debinding vaporized the rest polymer. During the chemical debinding, green parts (after molding) were subsequently immersed in n-hexane (VWR CHEMICALS, USA) at 40 °C for 15 h by using a LRA/EBA 50 debinding device (LÖMI, Germany). Thermal debinding (under argon flow (purity 99.996%, Linde Gas, Germany) below 600 °C) and sintering (1500 °C /4 h in vacuum of 10^{-5} mbar with

10 K/min cooling rate with Y_2O_3 sintering-support were continuously carried out in a debinding-sintering integrated furnace (XERION, Germany). This cold-wall furnace was equipped with tungsten heating elements and shield packs of molybdenum, and a vacuum burn-out/burn-off program was carried out, in order to keep impurity contamination as low as possible.

2.2. Microstructural characterization

The densities and porosities of the as-sintered MIM-parts were determined by the Archimedes' principle specified in ASTM B962 using an electronic balance (Sartorius AG, Germany). The theoretical compact densities were calculated considering the density of each element and its volume fraction [50]. The impurity levels with respect to carbon, nitrogen and oxygen were determined for six samples of each alloy by inert gas fusion technique (LECO TC436/CS444, USA). The oxygen equivalent, $O_{eq.}$, was calculated from the mean value of the measurements by Eq. (1) [51]. C_C, C_N and C_O denote the content of carbon, nitrogen and oxygen, respectively.

$$O_{eq.} = \frac{3}{4}C_C + 2C_N + C_O \quad (1)$$

In addition to the total $O_{eq.}$, the values of partial $O_{eq.}$ for carbon and nitrogen of all Ti2010-xY alloys were also calculated, as represented by blue symbols in Figure 1. The solid solution

oxygen equivalent, $O_{sseq.}$, was estimated by Eq. (2), assuming that the scavenging of oxygen by yttrium particles follows a certain ratio of yttrium to oxygen reported in literature, i.e. 0.1 wt.% yttrium to react with 0.027 wt.% oxygen [42]. C_Y denotes the concentration of yttrium.

$$O_{sseq.} = O_{eq.} - \ 0.27 \ \times \ C_Y \tag{2}$$

For the microstructure analysis, the specimens cut from as-sintered parts were polished and partially etched with "Kroll Reagent". Images of the microstructure were taken using an Olympus PMG-3 light microscope and a scanning electron microscopy (Tescan Vega3 SB, Czech Republic) equipped with energy dispersive spectrometer (EDS). The weight percentages of yttria particles were calculated from the chemical element mappings by using Iridium Ultra software. In addition, the particle size of yttria and area fraction of TiC were analysed by ImageJ from three SEM-images and optical images, respectively. The measurement of the prior β-grain size was conducted on etched samples by the software Olympus analysis Pro, and three images were taken for each condition. In order to estimate the mean diameter and form factor of porosity, three images containing approximately 150 pores in total were further analysed by ImageJ software. For analyzing the irregular degree of porosity, the shape of pores was defined by Eq. (3) [52, 53]. A form factor of 1 represents a circular pore in the planar view.

$$Form \ \ factor = \left(\sqrt{\frac{area}{\pi}} \times \frac{2\pi}{perimeter}\right)^2 \tag{3}$$

2.3. Tensile test

The tensile tests were performed in air at ambient temperature on a Schenck Trebel RM-100 tensile testing machine with a traverse speed of 0.5 mm/min. The gauge length was 30 mm and the gauge diameter 4.2 mm. The engineering strain was measured by a laser extensometer (Fiedler laser scanner, Germany). The tensile properties were determined for three non-post-treated (i.e. without shot peening and polishing) as-sintered MIM-parts from each Ti2010-xY alloy with different yttrium concentration. The area underneath the engineering stress-strain curves was calculated as tensile toughness by using OriginLab software.

3. Results and discussion

3.1. Influence of yttrium on chemical variation

Impurity levels in the MIM-processed Ti2010-xY alloys (x = 0, 0.3, …, 1) are summarized in Table 1. It reveals that the alloys differ only slightly in the content of C, N and O. It is also worth mentioning that NRC-IMI laboratory has found that even if the elemental analysis test by inert gas fusion method is performed under a good training and monitoring condition, the experimental error of LECO device is still as high as 4.4% (a relative deviation of 1.5% of measured values is given by the manufacturer) [35]. This is higher than the variance values in Table 1. The calculated oxygen equivalent values ($O_{eq.}$) of these MIM-processed Ti2010-xY alloys (see Figure 1) are basically unchanged.

The corresponding $O_{sseq.}$, however, changes due to the formation of yttria particles (Y_2O_3) and the resultant reduction in solid solution oxygen (Dissolved-O) in the Ti-matrix (Figure 1). It is noted that, after adding 1 wt.% yttrium, the solid solution oxygen equivalent ($O_{sseq.}$) in the MIMed Ti2010-1Y is reduced by as much as almost 60% compared with the original Ti2010 without yttrium addition.

3.2. Influence of yttrium on microstructural features

Table 2 lists the important data for the as-sintered microstructure, including sintering densities, porosities, average pore diameter, pore form factor, β-grain size and titanium carbides (TiC) area fraction. The typical microstructures of the as-sintered MIM-Ti2010-xY alloys pictured by optical microscopy are shown in Figure 2, where the black-colored areas are the residual porosity and the gray-colored spots are TiC precipitates. As-sintered yttrium free Ti2010 (Figure 2 (a)) exhibits apparently less pores than the alloy variants with yttrium addition (Figure 2 (b)−(e)). More, larger and interconnected pores (marked by red triangles in Figure 2 (e)) appear in Ti2010-xY alloys with high concentrations of yttrium. The detailed mechanism of TiC precipitation resulting from carbon contamination is described in the literature [34, 54-56].

The porosity features (incl. porosity size and form factor) of Ti2010-xY alloys with different

yttrium additions are plotted in Figure 3. A rather strong relationship is found between yttrium content and the porosity features. Adding 1 wt.% yttrium causes the sintering porosity fraction to rise by over 50% and the average pore diameter to increase by $\approx$35%, respectively, compared with the yttrium free alloy variant. On the other hand, as yttrium concentration increases, the overall pores tend to be more irregular, according to the calculated pore form factor.

It is well known that elimination of pores during sintering is caused by element diffusion driven by the minimization of particle surface energy [57, 58]. Refractory elements such as Nb can increase porosity owing to their slow diffusion rates even at elevated temperatures [49]. The reason for the decreased density in the Y-added samples, however, is different. It is generally accepted that yttrium is extremely active with oxygen. The effect of oxygen scavenging from the Ti-matrix accelerates dramatically in the range of 800 °C to 900 °C during heating of sintering cycle. This effect thoroughly ends at 1025 °C and as all elemental yttrium is consumed at that point [59]. Therefore, during sintering of the Y-added Ti2010 at high temperature, yttrium powder particles should only exist in the form of yttria (Y_2O_3) particles. Unlike the Ti, Nb and Zr atoms, yttrium atoms do not participate in large-scale elemental diffusion. Instead, based on the stable chemical structure of yttria (Cubic cI80 crystal structure [60]), the effect of yttrium on elemental diffusion may be negative, e.g. to obstruct the pore closing during sintering in Figure 5 (c), indicating its effective shielding effect on materials diffusion.

Regarding morphology and distribution of the yttria particles, Figure 4 and Figure 5 provide high and low magnification SEM-BSE images, respectively. It is discovered that yttria particles distribute either in the interior of the Ti-matrix (denoted as interior-yttria) or close to the pores (pore-yttria). In order to determine their chemical composition, an EDS mapping analysis is shown in Figure 4. From sample preparation some metal debris can be deposited in larger pores which is encircled by a dashed line. Yttrium and oxygen contrasts are readily detectable, regardless of stemming either from interior-yttria or from pore-yttria. Since no significant difference between these two kinds of yttria is visible, they are considered as compositional equal, suggesting only one type of Y-O oxide is formed. Furthermore, the Ti, Nb and Zr concentrations are considerably deficient in the yttria particles (see Figure 4). This result is in good agreement with the previous research that no Y-titanate such as $Y_2Ti_2O_7$ and Y_2TiO_5 was found in Y-added Ti-6Al-4V alloys by high-energy X-ray diffraction [59]. It further implies that yttria may have hindered the elemental diffusion and pore closing during sintering. However, the size and amount of interior-yttria are small, thus, it is unclear how large this effect actually is.

To unveil the effect of particle size of yttria on residual porosity, the particle size distributions of interior-yttria and pore-yttria were investigated. The results are given in Figure 5 (b). Before

yttrium reacts with oxygen to form yttria (i.e. the sintering cycle reaches about 800−900 °C), the solubility of yttrium in the Ti-matrix is very low with less than 0.02 wt.% [61]. Since early-formed yttria is rather stable during sintering, no yttria larger than the starting yttrium powder size (<45 μm) can be found. Therefore, it is reasonable to assume that yttrium powder hardly undergoes mass diffusion in the course of sintering, and the particle size of yttria in the as-sintered microstructure could represent the original yttrium powder particle size. From the results of the pore-yttria and interior-yttria, yttria particles of large size (e.g. ≈23 μm) are more likely to cause porosity. Meanwhile, the interior-yttria particles are below 15 μm. These findings suggest that the usage of larger yttrium particles should be avoided; however, a size of below 15 μm may be acceptable with respect to residual porosity.

Figure 6 indicates a significant difference between β-grain size of the yttrium free Ti2010 alloy variant and that of the Ti2010 alloys with yttrium addition. Even a small amount of yttrium (0.3 wt.%) can cause a significant grain refinement effect by approximately 40%. The reduction of prior β-grain size is likely attributed to two kinds of refinement mechanisms caused by the formation of yttria phases. From the inspection of micrographs of Ti2010-xY alloys, only the pore-yttria (large yttria combined with porosity) is present at the grain boundaries (GBs), and few separate interior-yttria located at GBs are discovered (see Figure 5 (d)). It is thus plausible that the early-formed interior-yttria act as additional nucleation sites, whereas large pore-yttria particles associated with porosity work as β-grain growth inhibitors. Because the number of

yttria particles depends on the yttrium concentration, the Ti2010-1Y alloy exhibits the finest grain size. The refined microstructure in turn should have an impact on the mechanical performance, which will be detailed in Section 3.3.

Figure 7 shows the carbon content and area fraction of the TiC second-phase in the Ti2010-xY alloys. It is noted that an increase of Y concentration has no significant effect on the fraction of the TiC phase or carbon solubility in the Ti-matrix. It can be inferred that at room temperature solid solution oxygen (dissolved-O) has no influence on the carbon solubility, even though more interstitial vacancies are present due to oxygen atoms being scavenged by yttrium.

3.3. Influence of yttrium on tensile properties

Tensile properties of the MIM-processed Ti2010-xY biomaterials are summarized in Table 3. The increase in porosity reduces the effective cross-sectional area for load bearing, leading to a reduction in strength and Young's modulus [62]. This decrease in Young's modulus is in general agreement with a previous study [63]. Yttria (Y_2O_3), although its Young's modulus is as high as 170 GPa [64], does not increase the overall Young's modulus. Instead, the measured Young's modulus values of Ti2010-xY alloys ($\approx$67 GPa) are rather low compared to other titanium alloys [65], which is beneficial to avoid the "stress-shielding" effect in orthopaedic applications [66].

The results shown in Table 3 of the mechanical properties (yield strength (YS), ultimate tensile strength (UTS), elongation (ε_f) and tensile toughness) are plotted in Figure 8 (a) and (b). The tensile strength decreases monotonously with increase of the yttrium concentration. At first glance, this decrease is surprising, since a more refined microstructure is found in the Ti2010 alloys with yttrium addition. However, the grain size appears not to contribute in this case. The most likely reason is the evidently increased porosity as well as reduced solid solution strengthening by interstitially dissolved oxygen, which overcompensates any positive effects of the smaller grain size. Ductility (Figure 8 (a)) and tensile toughness (Figure 8 (b)) show a similar tendency. Scavenging of oxygen by Y addition can improve the ductility of MIMed Ti2010-xY. However, excessively high porosity (more than 6%) and the presence of interconnected pores largely degrade the ductility as well as the fracture toughness if the yttrium concentration is increased too much. A reduced ductility caused by an excess amounts of Y can completely obliterate the enhancement of the deformation capability of the Ti-lattice that otherwise will benefit from oxygen scavenging.

A more detailed analysis is conducted as follows. As aforementioned, these alloys have nearly the same oxygen equivalent $O_{eq.}$ (approximaterly 0.45 wt.%, see Figure 1). Moreover, the particle strengthening effect at ambient temperature provided by moderate-sized RE oxides has

been found to be fairly limited [20]. Therefore, only solid solution oxygen equivalent ($O_{sseq.}$), relative density and prior β-grain size are taken into consideration. To determine their separate impacts the UTS of the alloys is plotted versus $O_{sseq.}$, relative density and the prior β-grain size (Figure 9). The reference materials also shown in Figure 9 are selected from refs. [16, 23, 67] for MIM Ti-6Al-4V and ref. [68] for MIM Ti-6Al-7Nb. There is an apparent linear relationship between UTS and solid solution oxygen equivalents as obvious from Figure 9 (a). Such results are consistent with literature [23, 68]. In those studies, linear relationships between oxygen equivalent in solid solution and tensile strength are also found, and no obvious oxide particles were present.

Meanwhile, it has been widely accepted that a decline in relative density (or increase in residual porosity) weakens tensile strength. Figure 9 (b) indicates that the strength-reducing effect (i.e. slope of the curve in the range of 93.5%−95% relative density) is in good agreement with the trend in MIM Ti-6Al-4V [23], as shown by the red line. However, with a higher porosity from 92.5% to 93.5%, there is an accelerating trend, deviating from the original linear relationship. This behavior is likely caused by excessive interconnected porosity that is more detrimental and reduces tensile strength to a greater extent. Interestingly, the beneficial effect of grain refinement on strength is not evident (see Figure 9 (c)). Note that this merely could imply that strengthening by grain refinement due to Y additions is overcompensated by the effects of residual porosity and solid solution oxygen equivalent. Therefore, a behavior according to the

classic Hall–Petch relationship was not detected [69, 70]. The previous studies, where MIMed Ti-6Al-4V with similar porosities (2.3%−3.6%) and oxygen contents (0.19 wt.% to 0.23 wt.%) was fabricated, as shown by red hexagons in Figure 9 (c) [16, 23, 67], weakly reflect the trend based on the Hall–Petch relationship, but with a fairly wide scatter band. To some extent, this is in general agreement with the present study, i.e. the effect is not clearly evident. In brief, it is reasonable to deduce that even if the prior β-grains are refined to only half of their original grain diameter, Hall–Petch strengthening is negligible in the range of grain sizes investigated here (e.g. 180−380 μm) if compared to effects of solid solution oxygen equivalent or residual porosity.

4. Conclusions

In the present study, biomedical β Ti-Nb-Zr alloys with varying Y additions were fabricated by metal injection molding. The effects of Y-induced oxygen scavenging, microstructure refinement and increased porosity on tensile properties were systematically investigated. The following conclusions can be drawn:

- The addition of Y with a particle size of more than ≈15 μm leads to an increase in residual porosity and causes irregular and interconnected pores in the MIM-prepared Ti-Nb-Zr alloys. The large-sized yttrium is believed to form pore-area yttria which hinder elemental diffusion at elevated temperatures preventing pore closing. Grain boundary

pinning by yttria was not found in this study. To scavenge oxygen from the Ti-matrix, Y elemental powder with a maximum particle size of less than 15 μm (e.g. 12 μm or 1200 mesh) is more appropriate and without significant detrimental effects on the as-sintered density.

- When the concentration of yttrium powder of a large particle size is more than 0.5 wt.%, degradation of ductility caused by excessive porosity becomes significant.

- Y addition generally degrades the tensile strength, proportional to the Y concentration introduced. This degradation is mainly resulting from the increase in overall porosity and irregular pores, and the decrease in the solid-solution state oxygen (dissolved-O). Although a grain size refinement is quite obvious (down to 187 μm from 373 μm), a beneficial effect of it on tensile strength was not found.

- Y addition in Ti-Nb-Zr alloys causes no observable effect on the area fraction of the TiC phase; in other words, oxygen concentration has no practical effect on carbon solubility at ambient temperature.

Acknowledgments: This research was supported by Helmholtz-Zentrum Geesthacht Zentrum für Material- und Küstenforschung. The authors would like to thank all those that actively contributed to realization of this work: A. Dobernowsky, W. Limberg, Dr. A. A. Hidalgo, P. Fischer, D. Matthiessen, Dr. J. Paul, K. Erdmann and S. Riekehr. In addition, P. Xu thanks the financial support of China Scholarship Counsil. Dr. M. Yan also appreciates the support of Humboldt Research Fellowship for Experienced Researchers.

Data availability

The raw/processed data required to reproduce these findings cannot be shared at this time as the data also forms part of an ongoing study.

References

[1] K. Xia, X. Wu, D. Song, Effects of Gd addition, lamellar spacing and loading direction on creep behaviour of a fully lamellar Ti–44Al–1Mn–2.5Nb alloy, Acta Materialia 52(4) (2004) 841-849. https://doi.org/10.1016/j.actamat.2003.10.018.

[2] Y.S. Tian, C.Z. Chen, L.X. Chen, Q.H. Huo, Effect of RE oxides on the microstructure of the coatings fabricated on titanium alloys by laser alloying technique, Scripta Materialia 54(5) (2006) 847-852. https://doi.org/10.1016/j.scriptamat.2005.11.011.

[3] Z. Hu, Y. Zhan, G. Zhang, J. She, C. Li, Effect of rare earth Y addition on the microstructure and mechanical properties of high entropy AlCoCrCuNiTi alloys, Materials & Design 31(3) (2010) 1599-1602. https://doi.org/10.1016/j.matdes.2009.09.016.

[4] L. Chen, X. Ma, L. Wang, X. Ye, Effect of rare earth element yttrium addition on microstructures and properties of a 21Cr–11Ni austenitic heat-resistant stainless steel, Materials & Design 32(4) (2011) 2206-2212. https://doi.org/10.1016/j.matdes.2010.11.022.

[5] M. Bugnet, A. Kula, M. Niewczas, G.A. Botton, Segregation and clustering of solutes at grain boundaries in Mg–rare earth solid solutions, Acta Materialia 79 (2014) 66-73. https://doi.org/10.1016/j.actamat.2014.06.004.

[6] E. Willbold, X. Gu, D. Albert, K. Kalla, K. Bobe, M. Brauneis, C. Janning, J. Nellesen, W. Czayka, W. Tillmann, Y. Zheng, F. Witte, Effect of the addition of low rare earth elements (lanthanum, neodymium, cerium) on the biodegradation and biocompatibility of magnesium, Acta Biomaterialia 11 (2015) 554-562. https://doi.org/10.1016/j.actbio.2014.09.041.

[7] Y. Liu, L.F. Chen, H.P. Tang, C.T. Liu, B. Liu, B.Y. Huang, Design of powder metallurgy titanium alloys and composites, Materials Science and Engineering: A 418(1) (2006) 25-35. https://doi.org/10.1016/j.msea.2005.10.057.

[8] H. Liu, Y. Gao, Y.M. Zhu, Y. Wang, J.F. Nie, A simulation study of β1 precipitation on dislocations in an Mg–rare earth alloy, Acta Materialia 77 (2014) 133-150. https://doi.org/10.1016/j.actamat.2014.04.054.

[9] P. Hidalgo-Manrique, J.D. Robson, M.T. Pérez-Prado, Precipitation strengthening and reversed yield stress asymmetry in Mg alloys containing rare-earth elements: A quantitative study, Acta Materialia 124 (2017) 456-467. https://doi.org/10.1016/j.actamat.2016.11.019.

[10] D.G. Konitzer, B.C. Muddle, H.L. Fraser, A comparison of the microstructures of as-cast and laser surface melted Ti-8Al-4Y, Metallurgical Transactions A 14(10) (1983) 1979-1988. https://doi.org/10.1007/BF02662365.

[11] Y. Chen, F. Kong, J. Han, Z. Chen, J. Tian, Influence of yttrium on microstructure, mechanical properties and deformability of Ti–43Al–9V alloy, Intermetallics 13(3) (2005) 263-266. https://doi.org/10.1016/j.intermet.2004.07.014.

[12] H. Tang, S. Lu, W. Jia, G. Yang, M. Qian, Selective electron beam melting of titanium and titanium aluminide alloys, International Journal of Powder Metallurgy 50(1) (2014) 57-64.

[13] W. Limberg, T. Ebel, K. Kainer, Addition of rare earth elements to MIM-processed TiAl6V4, European Congress and Exhibition on Powder Metallurgy. European PM Conference

Proceedings, The European Powder Metallurgy Association, 2014.
[14] W.F. Cui, C.M. Liu, L. Zhou, G.Z. Luo, Characteristics of microstructures and second-phase particles in Y-bearing Ti-1100 alloy, Materials Science and Engineering: A 323(1) (2002) 192-197. https://doi.org/10.1016/S0921-5093(01)01362-4.
[15] M.J. Bermingham, S.D. McDonald, M.S. Dargusch, D.H. StJohn, Grain-refinement mechanisms in titanium alloys, Journal of Materials Research 23(1) (2008) 97-104. https://doi.org/10.1557/JMR.2008.0002.
[16] W. Limberg, T. Ebel, Metal injection moulding of Ti-6Al-4V with yttrium addition, Key Engineering Materials 704 (2016) 20-27. https://doi.org/10.4028/www.scientific.net/KEM.704.20.
[17] C. Zhang, F. Yang, Z. Guo, H. Wang, B. Lu, Oxygen scavenging, grain refinement and mechanical properties improvement in powder metallurgy titanium and titanium alloys with CaB6, Powder Technology 340 (2018) 362-369. https://doi.org/10.1016/j.powtec.2018.09.054.
[18] O.M. Ferri, T. Ebel, R. Bormann, The influence of a small boron addition on the microstructure and mechanical properties of Ti-6Al-4V fabricated by metal injection moulding, Advanced Engineering Materials 13(5) (2011) 436-447. https://doi.org/10.1002/adem.201000280.
[19] Y. Liu, L. Chen, W. Wei, H. Tang, B. Liu, B. Huang, Improvement of ductility of powder metallurgy titanium alloys by addition of rare earth element, Journal of Materials Science & Technology 22(4) (2006) 465-469.
[20] Y. Liu, Y.B. Liu, B. Wang, H. Tang, Rare earth element: Is it a necessity for PM Ti alloys?, Key Engineering Materials 520 (2012) 41-48. https://doi.org/10.4028/www.scientific.net/KEM.520.41.
[21] Y.F. Yang, S.D. Luo, G.B. Schaffer, M. Qian, Impurity scavenging, microstructural refinement and mechanical properties of powder metallurgy titanium and titanium alloys by a small addition of cerium silicide, Materials Science and Engineering: A 573 (2013) 166-174. https://doi.org/10.1016/j.msea.2013.02.042.
[22] R. Gerling, E. Aust, W. Limberg, M. Pfuff, F.P. Schimansky, Metal injection moulding of gamma titanium aluminide alloy powder, Materials Science and Engineering: A 423(1) (2006) 262-268. https://doi.org/10.1016/j.msea.2006.02.002.
[23] T. Ebel, O. Milagres Ferri, W. Limberg, M. Oehring, F. Pyczak, F.P. Schimansky, Metal injection moulding of titanium and titanium-aluminides, Key Engineering Materials 520 (2012) 153-160. https://doi.org/10.4028/www.scientific.net/KEM.520.153.
[24] M. Yan, W. Xu, M.S. Dargusch, H.P. Tang, M. Brandt, M. Qian, Review of effect of oxygen on room temperature ductility of titanium and titanium alloys, Powder Metallurgy 57(4) (2014) 251-257. https://doi.org/10.1179/1743290114Y.0000000108.
[25] M. Yan, Y. Liu, Y.B. Liu, C. Kong, G.B. Schaffer, M. Qian, Simultaneous gettering of oxygen and chlorine and homogenization of the β phase by rare earth hydride additions to a powder metallurgy Ti–2.25Mo–1.5Fe alloy, Scripta Materialia 67(5) (2012) 491-494. https://doi.org/10.1016/j.scriptamat.2012.06.009.

[26] R. German, Progress in titanium metal powder injection molding, Materials 6(8) (2013) 3641-3662. https://doi.org/10.3390/ma6083641.
[27] D.F. Heaney, Handbook of metal injection molding, Woodhead Publishing, 2018.
[28] A. Dehghan-Manshadi, P. Yu, M. Dargusch, D. StJohn, M. Qian, Metal injection moulding of surgical tools, biomaterials and medical devices: A review, Powder Technology 364 (2020) 189-204. https://doi.org/10.1016/j.powtec.2020.01.073.
[29] A. Dehghan-Manshadi, M.J. Bermingham, M.S. Dargusch, D.H. StJohn, M. Qian, Metal injection moulding of titanium and titanium alloys: Challenges and recent development, Powder Technology 319 (2017) 289-301. https://doi.org/10.1016/j.powtec.2017.06.053.
[30] L. Bolzoni, E.M. Ruiz-Navas, E. Gordo, Quantifying the properties of low-cost powder metallurgy titanium alloys, Materials Science and Engineering: A 687 (2017) 47-53. https://doi.org/10.1016/j.msea.2017.01.049.
[31] M. Qian, Y.F. Yang, M. Yan, S.D. Luo, Design of low cost high performance powder metallurgy titanium alloys: Some basic considerations, Key Engineering Materials 520 (2012) 24-29. https://doi.org/10.4028/www.scientific.net/KEM.520.24.
[32] W. Ding, G. Chen, M. Qin, Y. He, X. Qu, Low-cost Ti powders for additive manufacturing treated by fluidized bed, Powder Technology 350 (2019) 117-122. https://doi.org/10.1016/j.powtec.2019.03.042.
[33] T. Ebel, V. Friederici, P. Imgrund, T. Hartwig, Metal injection molding of titanium, in: M. Qian, F.H. Froes (Eds.), Titanium Powder Metallurgy, Butterworth-Heinemann, Boston, 2015, pp. 337-360. https://doi.org/10.1016/B978-0-12-800054-0.00019-8.
[34] P. Xu, F. Pyczak, M. Yan, W. Limberg, R. Willumeit-Römer, T. Ebel, Tensile toughening of powder-injection-molded β Ti-Nb-Zr biomaterials by adjusting TiC particle distribution from aligned to dispersed pattern, Applied Materials Today 19 (2020) 100630. https://doi.org/10.1016/j.apmt.2020.100630.
[35] E. Baril, L.P. Lefebvre, Y. Thomas, Interstitial elements in titanium powder metallurgy: sources and control, Powder Metallurgy 54(3) (2011) 183-186. https://doi.org/10.1179/174329011X13045076771759.
[36] M. Abdel-Hady, K. Hinoshita, M. Morinaga, General approach to phase stability and elastic properties of β-type Ti-alloys using electronic parameters, Scripta Materialia 55(5) (2006) 477-480. https://doi.org/10.1016/j.scriptamat.2006.04.022.
[37] L.-F. Huang, B. Grabowski, J. Zhang, M.-J. Lai, C.C. Tasan, S. Sandlöbes, D. Raabe, J. Neugebauer, From electronic structure to phase diagrams: A bottom-up approach to understand the stability of titanium–transition metal alloys, Acta Materialia 113 (2016) 311-319. https://doi.org/10.1016/j.actamat.2016.04.059.
[38] T.H. Okabe, K. Hirota, E. Kasai, F. Saito, Y. Waseda, K.T. Jacob, Thermodynamic properties of oxygen in RE–O (RE=Gd, Tb, Dy, Er) solid solutions, Journal of Alloys and Compounds 279(2) (1998) 184-191. https://doi.org/10.1016/S0925-8388(98)00690-2.
[39] G.E. Thompson, P. Skeldon, X. Zhou, K. Shimizu, H. Habazaki, C.J.E. Smith, Improving the performance of aerospace alloys, Aircraft Engineering and Aerospace Technology 75(4)

(2003) 372-379. https://doi.org/10.1108/00022660310484301.
[40] M. Yan, H.P. Tang, M. Qian, Scavenging of oxygen and chlorine from powder metallurgy (PM) titanium and titanium alloys, in: M. Qian, F.H. Froes (Eds.), Titanium Powder Metallurgy, Butterworth-Heinemann, Boston, 2015, pp. 253-276. https://doi.org/10.1016/B978-0-12-800054-0.00015-0.
[41] I. Barin, O. Knacke, O. Kubaschewski, Thermochemical properties of inorganic substances: supplement, Springer Science & Business Media, 2013.
[42] W. Limberg, R. Willumeit, F. Pyczak, T. Ebel, Metal injection moulding (MIM) of Ti-6Al-4V HDH-powder with high oxygen content, achieving high strength and high ductility by addition of yttrium, European Congress and Exhibition on Powder Metallurgy. European PM Conference Proceedings, The European Powder Metallurgy Association, 2018.
[43] F.H. Froes, D. Eylon, Powder metallurgy of titanium alloys, International Materials Reviews 35(1) (1990) 162-184. https://doi.org/10.1179/095066090790323984.
[44] N. Kurgan, Effect of porosity and density on the mechanical and microstructural properties of sintered 316L stainless steel implant materials, Materials & Design 55 (2014) 235-241. https://doi.org/10.1016/j.matdes.2013.09.058.
[45] Z.Z. Fang, J.D. Paramore, P. Sun, K.S.R. Chandran, Y. Zhang, Y. Xia, F. Cao, M. Koopman, M. Free, Powder metallurgy of titanium – past, present, and future, International Materials Reviews 63(7) (2018) 407-459. https://doi.org/10.1080/09506608.2017.1366003.
[46] O.M. Ferri, T. Ebel, R. Bormann, High cycle fatigue behaviour of Ti–6Al–4V fabricated by metal injection moulding technology, Materials Science and Engineering: A 504(1) (2009) 107-113. https://doi.org/10.1016/j.msea.2008.10.039.
[47] W. Limberg, T. Ebel, F. Pyczak, M. Oehring, F.P. Schimansky, Influence of the sintering atmosphere on the tensile properties of MIM-processed Ti 45Al 5Nb 0.2B 0.2C, Materials Science and Engineering: A 552 (2012) 323-329. https://doi.org/10.1016/j.msea.2012.05.047.
[48] F. Kafkas, T. Ebel, Metallurgical and mechanical properties of Ti–24Nb–4Zr–8Sn alloy fabricated by metal injection molding, Journal of Alloys and Compounds 617 (2014) 359-366. https://doi.org/10.1016/j.jallcom.2014.07.168.
[49] D. Zhao, K. Chang, T. Ebel, H. Nie, R. Willumeit, F. Pyczak, Sintering behavior and mechanical properties of a metal injection molded Ti–Nb binary alloy as biomaterial, Journal of Alloys and Compounds 640 (2015) 393-400. https://doi.org/10.1016/j.jallcom.2015.04.039.
[50] M. Holm, T. Ebel, M. Dahms, Investigations on Ti–6Al–4V with gadolinium addition fabricated by metal injection moulding, Materials & Design 51 (2013) 943-948. https://doi.org/10.1016/j.matdes.2013.05.003.
[51] R. German, Titanium powder injection moulding: a review of the current status of materials, processing, properties and applications, PIM International 3(4) (2009) 21-37.
[52] G.C. Obasi, O.M. Ferri, T. Ebel, R. Bormann, Influence of processing parameters on mechanical properties of Ti–6Al–4V alloy fabricated by MIM, Materials Science and Engineering: A 527(16) (2010) 3929-3935. https://doi.org/10.1016/j.msea.2010.02.070.
[53] J. Soyama, M. Oehring, W. Limberg, T. Ebel, K.U. Kainer, F. Pyczak, The effect of

zirconium addition on sintering behaviour, microstructure and creep resistance of the powder metallurgy processed alloy Ti–45Al–5Nb–0.2B–0.2C, Materials & Design 84 (2015) 87-94. https://doi.org/10.1016/j.matdes.2015.06.095.
[54] M. Yan, M. Qian, C. Kong, M.S. Dargusch, Impacts of trace carbon on the microstructure of as-sintered biomedical Ti–15Mo alloy and reassessment of the maximum carbon limit, Acta Biomaterialia 10(2) (2014) 1014-1023. https://doi.org/10.1016/j.actbio.2013.10.034.
[55] X. Luo, T. Ebel, F. Pyczak, W. Limberg, Y. Lin, Carbide evolution and its potential reduction methods in Ti-22Nb based alloys prepared by metal injection moulding, Materials Letters 193 (2017) 295-298. https://doi.org/10.1016/j.matlet.2017.01.145.
[56] T. Ebel, T. Beißig, S. Ebner, X. Luo, A.B. Nagaram, D. Zhao, Reduction of the embrittlement effect of binder contamination in MIM processing of Ti alloys, Powder Metallurgy 60(3) (2017) 157-166. https://doi.org/10.1080/00325899.2017.1291085.
[57] R.M. German, Sintering Theory and Practice, Wiley-VCH, New York, 1996.
[58] F. Thomsen, T. Ebel, R. Willumeit-Römer, Simulation of neck growth and shrinkage for realistic temperature profiles – Determination of diffusion coefficients in a practical oriented procedure, Scripta Materialia 168 (2019) 108-113. https://doi.org/10.1016/j.scriptamat.2019.04.034.
[59] W. Limberg, R. Willumeit-Römer, F. Pyczak, T. Ebel, A. Stark, Enhancement of fatigue-properties of MIM-processed Ti-6Al-4V by addition of yttrium and characterization by in situ X-ray scattering, European Congress and Exhibition on Powder Metallurgy. European PM Conference Proceedings, The European Powder Metallurgy Association, 2017.
[60] Y.-N. Xu, Z. Gu, W.Y. Ching, Electronic, structural, and optical properties of crystalline yttria, Physical Review B 56(23) (1997) 14993-15000. https://doi.org/10.1103/PhysRevB.56.14993.
[61] A. International, A.I.A.P.D. Committee, A.I.H. Committee, ASM handbook, ASM International, 1992.
[62] K.A. Nazari, A. Nouri, T. Hilditch, Mechanical properties and microstructure of powder metallurgy Ti–xNb–yMo alloys for implant materials, Materials & Design 88 (2015) 1164-1174. https://doi.org/10.1016/j.matdes.2015.09.106.
[63] D. Zhao, K. Chang, T. Ebel, M. Qian, R. Willumeit, M. Yan, F. Pyczak, Microstructure and mechanical behavior of metal injection molded Ti–Nb binary alloys as biomedical material, Journal of the Mechanical Behavior of Biomedical Materials 28 (2013) 171-182. https://doi.org/10.1016/j.jmbbm.2013.08.013.
[64] W.R. Manning, O. Hunter Jr, B.R. Powell Jr, Elastic properties of polycrystalline yttrium oxide, dysprosium oxide, holmium oxide, and erbium oxide: room temperature measurements, Journal of the American Ceramic Society 52(8) (1969) 436-442. https://doi.org/10.1111/j.1151-2916.1969.tb11974.x.
[65] M. Niinomi, M. Nakai, J. Hieda, Development of new metallic alloys for biomedical applications, Acta Biomaterialia 8(11) (2012) 3888-3903. https://doi.org/10.1016/j.actbio.2012.06.037.

[66] M. Geetha, A.K. Singh, R. Asokamani, A.K. Gogia, Ti based biomaterials, the ultimate choice for orthopaedic implants – A review, Progress in Materials Science 54(3) (2009) 397-425. https://doi.org/10.1016/j.pmatsci.2008.06.004.
[67] O.M. Ferri, T. Ebel, R. Bormann, Influence of surface quality and porosity on fatigue behaviour of Ti–6Al–4V components processed by MIM, Materials Science and Engineering: A 527(7) (2010) 1800-1805. https://doi.org/10.1016/j.msea.2009.11.007.
[68] A.A. Hidalgo, T. Ebel, W. Limberg, F. Pyczak, Influence of oxygen on the fatigue behaviour of Ti-6Al-7Nb alloy, Key Engineering Materials 704 (2016) 44-52. https://doi.org/10.4028/www.scientific.net/KEM.704.44.
[69] E.O. Hall, The deformation and ageing of mild steel: III discussion of results, Proceedings of the Physical Society. Section B 64(9) (1951) 747-753. https://doi.org/10.1088/0370-1301/64/9/303.
[70] N. Petch, The cleavage strength of polycrystals, Journal of the Iron and Steel Institute 174 (1953) 25-28.

Table 1

Measured impurities levels of Ti2010-xY alloys (x = 0, 0.3, …, 1), oxygen equivalent ($O_{eq.}$) and calculated solid solution oxygen equivalent ($O_{sseq.}$) (unit: weight %).

Materials composition	C	O	N	$O_{eq.}$	$O_{sseq.}$[a]
Ti2010	0.047 ± 0.003	0.265 ± 0.001	0.082 ± 0.003	0.460	0.460
Ti2010-0.3Y	0.043 ± 0.001	0.266 ± 0.003	0.081 ± 0.014	0.457	0.376
Ti2010-0.5Y	0.049 ± 0.003	0.265 ± 0.009	0.081 ± 0.003	0.460	0.325
Ti2010-0.7Y	0.045 ± 0.004	0.253 ± 0.004	0.075 ± 0.004	0.433	0.244
Ti2010-1Y	0.050 ± 0.001	0.271 ± 0.010	0.077 ± 0.001	0.458	0.188

[a] *The solid solution oxygen equivalent, $O_{sseq.}$, was calculated by Eq. (2), according to 0.1 wt.% yttrium scavenging 0.027 wt.% oxygen from solid solution in the Ti-matrix. C_Y denotes the concentration of yttrium.*

$$O_{sseq.} = O_{eq.} - 0.27 \times C_Y \quad (2)$$

Table 2

Physical and microstructural properties of Ti2010-xY alloys.

Alloy	Sinter density (g/cm^3)	Porosity (%)	Average pore diameter (µm)	Average pore form factor (-)	Grain size (µm)	TiC (area fraction %)
Ti2010	4.89	5.0	14.2	0.64	373 ± 12	0.53 ± 0.05
Ti2010-0.3Y	4.82	6.5	16.6	0.58	222 ± 5	0.52 ± 0.02
Ti2010-0.5Y	4.80	6.9	17.5	0.56	212 ± 15	0.55 ± 0.07
Ti2010-0.7Y	4.77	7.3	18.9	0.53	201 ± 20	0.58 ± 0.06
Ti2010-1Y	4.75	7.7	19.1	0.51	187 ± 17	0.54 ± 0.11

Table 3

Tensile properties of Ti2010-xY alloys.

Alloy	Young's modulus (GPa)	Yield strength (MPa)	Ultimate tensile strength (MPa)	Elongation (%)	Toughness ($J \cdot mm^{-3}$)
Ti2010	71 ± 2.9	768 ± 3.9	889 ± 3.9	3.9 ± 0.5	39.3 ± 4.7
Ti2010-0.3Y	69 ± 2.5	715 ± 7.1	843 ± 4.8	5.0 ± 1.1	46.0 ± 8.1
Ti2010-0.5Y	67 ± 3.5	690 ± 3.3	816 ± 1.5	4.4 ± 0.6	40.0 ± 4.4
Ti2010-0.7Y	62 ± 2.7	649 ± 4.4	776 ± 5.3	4.1 ± 0.7	35.3 ± 4.7
Ti2010-1Y	61 ± 2.0	612 ± 7.5	738 ± 2.2	3.3 ± 0.6	28.1 ± 3.6

Figure 1:

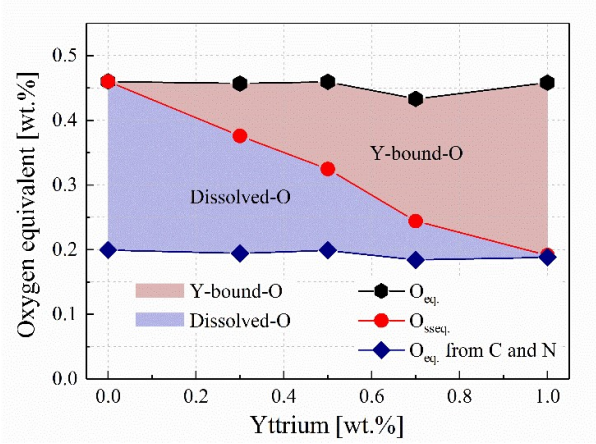

Figure 1 – The solid solution oxygen equivalent $O_{sseq.}$ (red symbols), oxygen equivalent $O_{eq.}$ from all interstitials (black) and oxygen equivalent $O_{eq.}$ from C and N alone (blue) in MIMed Ti2010-xY alloys with different yttrium weight fractions (x = 0, 0.3, …, 1). The light red-colored region represents how much oxygen has reacted with yttrium to form yttria and becomes Y-bound-O, whereas the light blue-colored region represents how much oxygen was in solid solution in the Ti-matrix (Dissolved-O).

Figure 2:

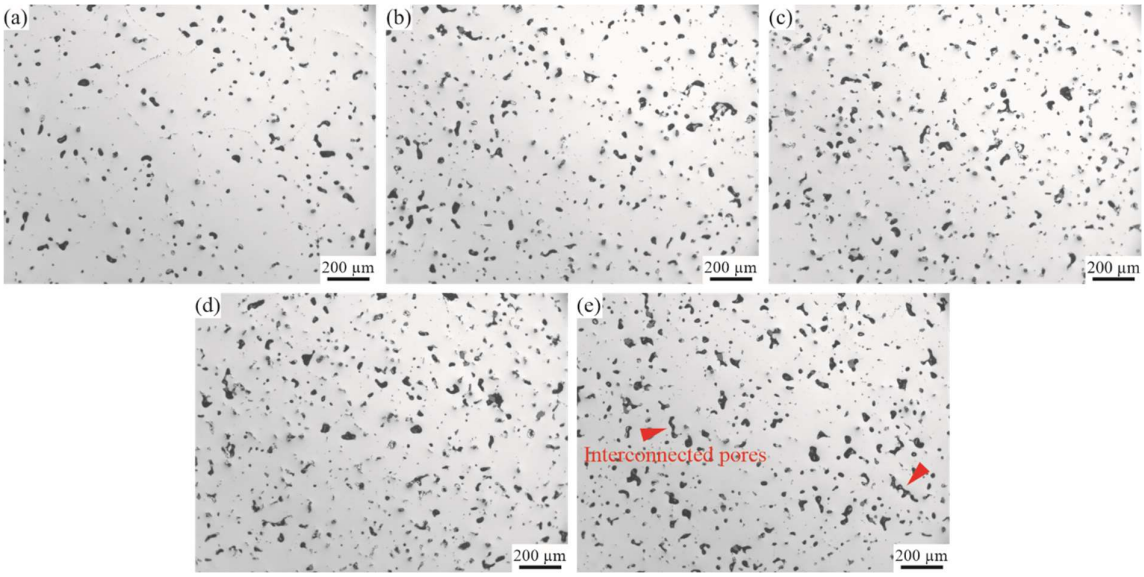

Figure 2 – Optical micrographs of Ti2010-xY alloys: (a) Ti2010; (b) Ti2010-0.3Y; (c) Ti2010-0.5Y; (d) Ti2010-0.7Y; and (e) Ti2010-1Y. The interconnected pores appear in high-Y-added Ti2010 alloys, marked by red triangles.

Figure 3:

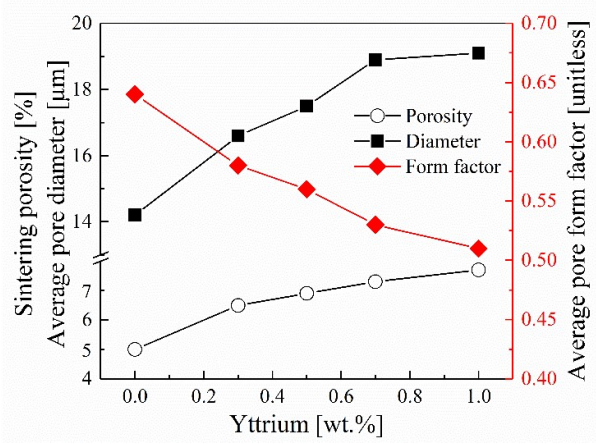

Figure 3 – Influence of yttrium concentration on the porosity features of the as-sintered Ti2010-xY alloys.

Figure 4:

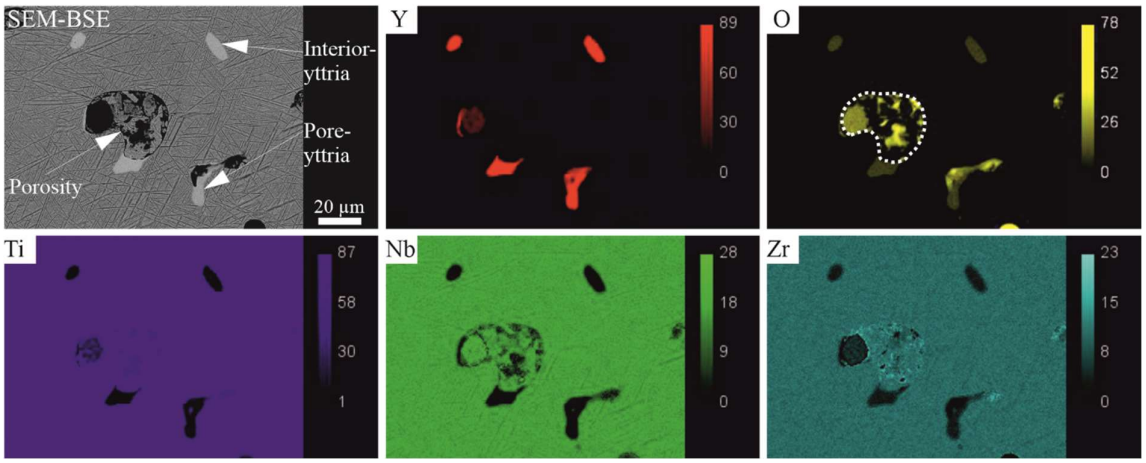

Figure 4 – SEM-BSE image and chemical element mappings of two kinds of yttria particles (interior-yttria and pore-yttria) in Ti2010-1Y alloy.

Figure 5:

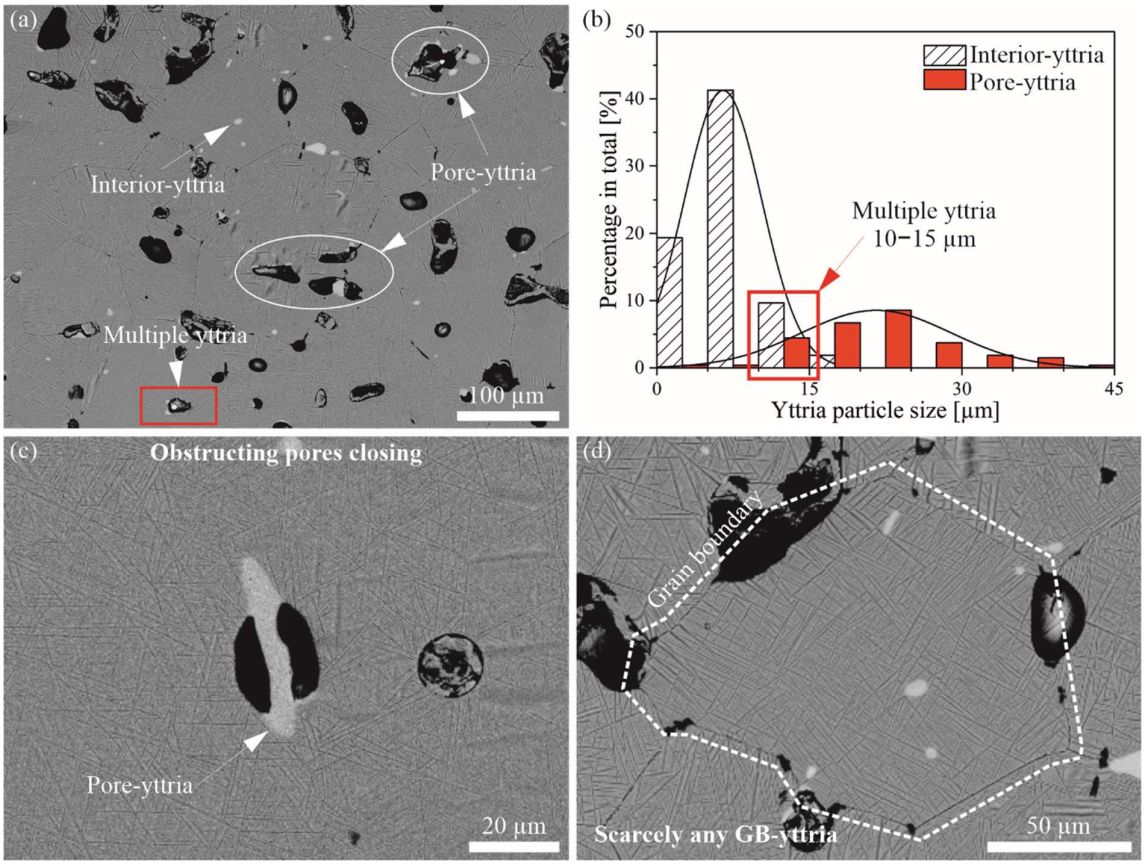

Figure 5 – SEM-images of two kinds of yttria and their particle size distribution. (a) Yttria distribution; (b) Particle size distributions of interior-yttria and pore-yttria, note that the small-sized pore-yttria, e.g. 10−15 µm, example marked by red rectangle in Figure 5 (a), usually are compounds of multiple yttria particles; (c) Typical large yttria obstructs pore closing; and (d) Individual yttria away from porosity pinning at GBs is hardly discovered.

Figure 6:

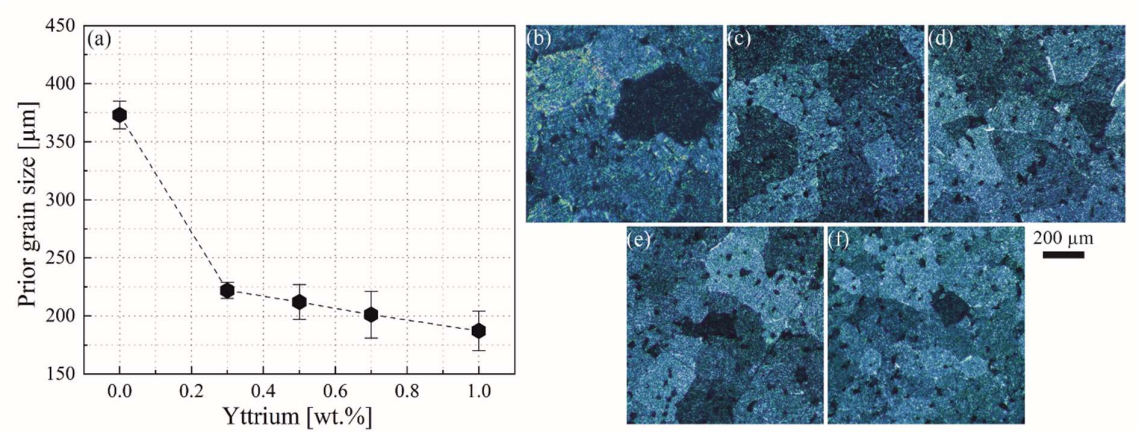

Figure 6 – Influence of yttrium on prior β-grain size of as-sintered Ti2010-xY alloys. (a) Mean value of prior β-grain size; Representative micrographs of etched specimens of (b) Ti2010; (c) Ti2010-0.3Y; (d) Ti2010-0.5Y; (e) Ti2010-0.7Y; and (f) Ti2010-1Y, indicating the change of grain size.

Figure 7:

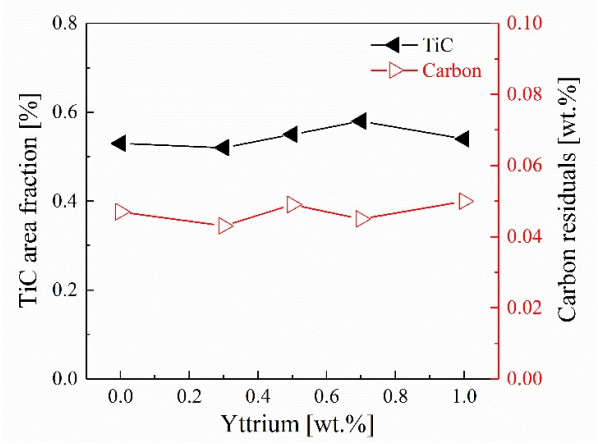

Figure 7 – Total carbon content and area fraction of the TiC precipitates in Ti2010-xY plotted vs. yttrium content.

Figure 8:

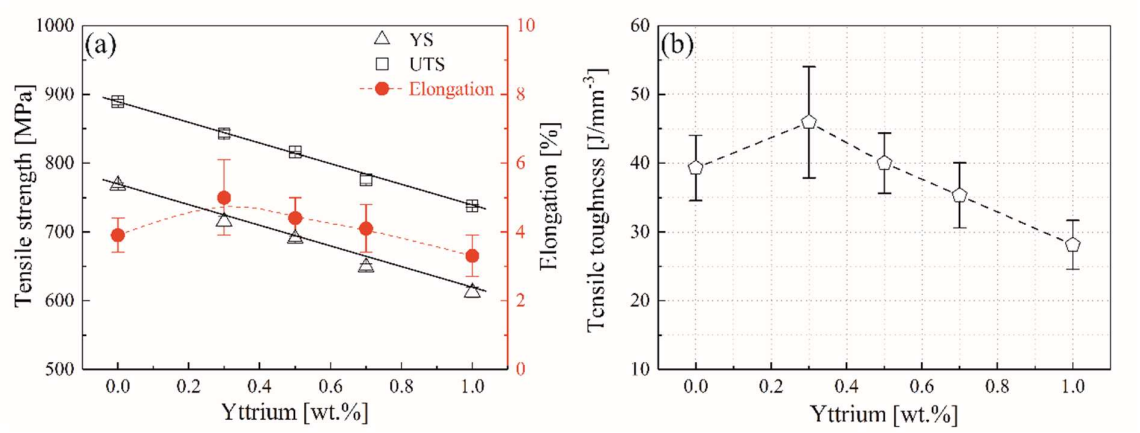

Figure 8 – (a) Influence of yttrium concentration on the tensile strength (incl. YS and UTS) and elongation to fracture (ε_f) of MIM-processed Ti2010-xY alloys; (b) Tensile toughness of Ti2010-xY alloys.

Figure 9:

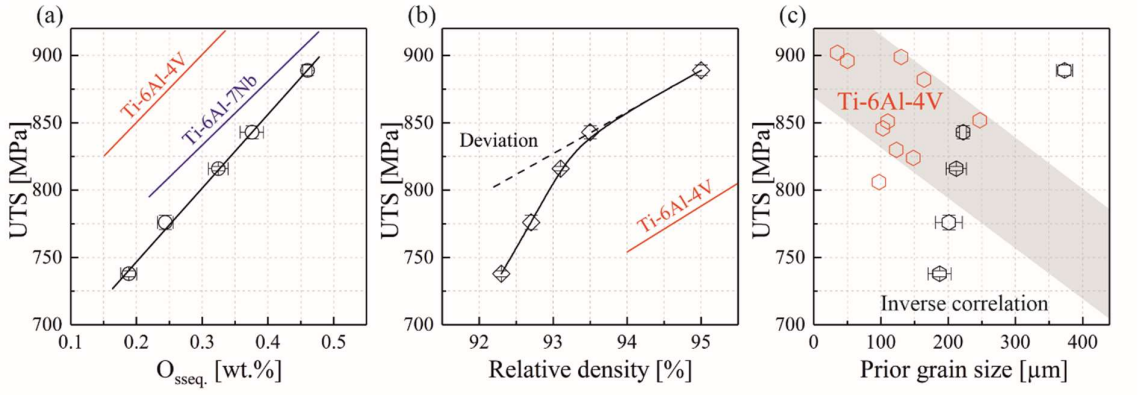

Figure 9 – The relationship of UTS and its possible impact factors: (a) vs. solid solution oxygen equivalent $O_{sseq.}$; (b) vs. relative density; and (c) vs. mean β-grain size. The reference materials are selected from refs. [16, 23, 67] for MIM Ti-6Al-4V and ref. [68] for MIM Ti-6Al-7Nb.